



Microstructure and Oxidation of a MAX Phase/Superalloy Hybrid Interface

James L. Smialek
Glenn Research Center, Cleveland, Ohio

Anita Garg
The University of Toledo, Toledo, Ohio

NASA STI Program . . . in Profile

Since its founding, NASA has been dedicated to the advancement of aeronautics and space science. The NASA Scientific and Technical Information (STI) program plays a key part in helping NASA maintain this important role.

The NASA STI Program operates under the auspices of the Agency Chief Information Officer. It collects, organizes, provides for archiving, and disseminates NASA's STI. The NASA STI program provides access to the NASA Aeronautics and Space Database and its public interface, the NASA Technical Reports Server, thus providing one of the largest collections of aeronautical and space science STI in the world. Results are published in both non-NASA channels and by NASA in the NASA STI Report Series, which includes the following report types:

- **TECHNICAL PUBLICATION.** Reports of completed research or a major significant phase of research that present the results of NASA programs and include extensive data or theoretical analysis. Includes compilations of significant scientific and technical data and information deemed to be of continuing reference value. NASA counterpart of peer-reviewed formal professional papers but has less stringent limitations on manuscript length and extent of graphic presentations.
- **TECHNICAL MEMORANDUM.** Scientific and technical findings that are preliminary or of specialized interest, e.g., quick release reports, working papers, and bibliographies that contain minimal annotation. Does not contain extensive analysis.
- **CONTRACTOR REPORT.** Scientific and technical findings by NASA-sponsored contractors and grantees.

- **CONFERENCE PUBLICATION.** Collected papers from scientific and technical conferences, symposia, seminars, or other meetings sponsored or cosponsored by NASA.
- **SPECIAL PUBLICATION.** Scientific, technical, or historical information from NASA programs, projects, and missions, often concerned with subjects having substantial public interest.
- **TECHNICAL TRANSLATION.** English-language translations of foreign scientific and technical material pertinent to NASA's mission.

Specialized services also include creating custom thesauri, building customized databases, organizing and publishing research results.

For more information about the NASA STI program, see the following:

- Access the NASA STI program home page at <http://www.sti.nasa.gov>
- E-mail your question to help@sti.nasa.gov
- Fax your question to the NASA STI Information Desk at 443-757-5803
- Phone the NASA STI Information Desk at 443-757-5802
- Write to:
STI Information Desk
NASA Center for AeroSpace Information
7115 Standard Drive
Hanover, MD 21076-1320



Microstructure and Oxidation of a MAX Phase/Superalloy Hybrid Interface

James L. Smialek
Glenn Research Center, Cleveland, Ohio

Anita Garg
The University of Toledo, Toledo, Ohio

National Aeronautics and
Space Administration

Glenn Research Center
Cleveland, Ohio 44135

Acknowledgments

The authors are grateful to Donald Humphrey for producing the hot pressed samples, Joy Buehler for metallography, and Tim Gabb and Chantal Sudbrack for helpful discussions.

Trade names and trademarks are used in this report for identification only. Their usage does not constitute an official endorsement, either expressed or implied, by the National Aeronautics and Space Administration.

This work was sponsored by the Fundamental Aeronautics Program at the NASA Glenn Research Center.

Level of Review: This material has been technically reviewed by technical management.

Available from

NASA Center for Aerospace Information
7115 Standard Drive
Hanover, MD 21076-1320

National Technical Information Service
5301 Shawnee Road
Alexandria, VA 22312

Available electronically at <http://www.sti.nasa.gov>

Microstructure and Oxidation of a MAX Phase/Superalloy Hybrid Interface

James L. Smialek
National Aeronautics and Space Administration
Glenn Research Center
Cleveland, Ohio 44135

Anita Garg
The University of Toledo
Toledo, Ohio 43606

Abstract

Corrosion resistant, strain tolerant MAX phase coatings are of interest for turbine applications. Thin Cr_2AlC MAX phase wafers were vacuum diffusion bonded to an advanced turbine disk alloy, LSHR, at 1100°C . The interface, examined by optical and scanning electron microscopy, revealed a primary diffusion zone consisting of $\sim 10\text{ }\mu\text{m}$ of $\beta\text{-Ni}(\text{Co})\text{Al}$, decorated with various NiCoCrAl , MC and M_3B_2 precipitates. On the Cr_2AlC side, an additional $\sim 40\text{ }\mu\text{m}$ Al-depletion zone of Cr_7C_3 formed in an interconnected network with the $\beta\text{-Ni}(\text{Co})\text{Al}$. Oxidation of an exposed edge at 800°C for 100 h produced a fine-grained lenticular alumina scale over Cr_2AlC and $\beta\text{-Ni}(\text{Co})\text{Al}$, with coarser chromia granules over the Cr_7C_3 regions. Subsequent growth of the diffusion layers was only $\sim 5\text{ }\mu\text{m}$ in total. A residual stress of $\sim 500\text{ MPa}$ was estimated for the MAX phase layer, but no interfacial damage was observed. Subsequent tests for 1000 h reveal similar results.

Introduction

M-A-X compounds are carbide or nitride ceramics well known for their unique behavior as ‘deformable’ and ‘strain tolerant’ ceramics. This property arises from the special hexagonal crystal structure that contains weakly bonded (0003) hkil crystallographic planes (Barsoum & El-raghy, 2001) (Eklund, Beckers, Jansson, Högberg, & Hultman, 2010). These can deform by sliding and kinking rather than by the macroscopic cracking and cleavage typical of most ceramics. The chemistry is generically described as M = group III-VI transition metals (Sc, Ti, V, Cr); A = group IIIA –VA main elements (Al, Si, Ge, P); and X = C, N. The stoichiometry is commonly M_2AX , M_3AX_2 , or M_4AX_3 . The structure is distinguished by planes of A-group elements every 3rd, 4th, or 5th layer, respectively, in a global M_{n+1}X_n lattice. While many of the M-X ceramic properties are maintained (high melting, high modulus, high strength), the relatively weak M-A and A-X bonds allow for easy intercalated planar delamination that results in high strain tolerance. This produces unique aspects such as high machinability, fracture toughness, thermal fatigue resistance, and coefficient of thermal expansion for an otherwise ‘ceramic-like’ material.

While there have been over 60 MAX phases identified, those containing Al have the potential of excellent oxidation resistance owing to the formation of Al_2O_3 scales (Tallman, Anasori, & Barsoum, 2013). These include Ti_2AlN , Ti_3AlC_2 , Ti_2AlC , and Cr_2AlC , the latter two exhibiting among the highest oxidation resistance (Wubian Tian, Wang, Kan, & Zhang, 2008) (Z. J. Lin, Li, Wang, & Zhou, 2007) (D.B. Lee, Nguyen, Han, & Park, 2007). In general these studies have found alumina scale growth rates in the range of those formed on oxidation resistant NiAl or FeCrAl alloys, with good oxidation resistance up

to 1300 °C for Ti_3AlC_2 and Ti_2AlC and 1200 °C for Cr_2AlC (Tallman et al., 2013). Ti_2AlC has been characterized as having good cyclic oxidation resistance because of its good thermal expansion match to that of the alumina scale. The higher CTE of Cr_2AlC leads to an increased spallation tendency similar to that observed for metals, but at much higher temperatures.

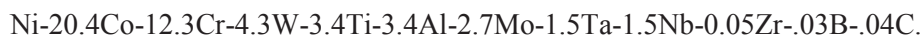
Furthermore, studies document good corrosion resistance of Ti_3AlC_2 and Cr_2AlC in SO_2 environments (Dong Bok Lee & Park, 2011) (Dong Bok Lee, Nguyen, & Park, 2011). Also, hot corrosion resistance was demonstrated in molten Na_2SO_4 salt for Cr_2AlC (Z. Lin, Zhou, Li, & Wang, 2006a), and for Ti_3AlC_2 , but only if preoxidized (Z. Lin, Zhou, Li, & Wang, 2006b). Thus the production of MAX phases as protective coatings for stainless steel, Ni-base superalloy M38G, Ti6242, and TiAl substrates has been demonstrated, primarily via magnetron sputtering (Eklund et al., 2010) (Walter, Sigumonrong, El-Raghy, & Schneider, 2006) (Gulbiski, 2004) (Hajas et al., 2011) (Wang, Flores Renteria, et al., 2010) (Wang, Mykhaylonka, et al., 2010) (Li, Li, Xiang, Lu, & Zhou, 2011).

Emerging problem areas of environmental degradation in turbines are gas phase embrittlement, oxidation, and low temperature hot corrosion (LTHC) of advanced disk alloys used in the high pressure turbine stage. (Woodford, 2006) (Birbilis & Buchheit, 2008) (Sudbrack et al., 2012) (Encinas-Oropesa et al., 2008) (Sumner, Encinas-Oropesa, Simms, & Oakey, 2011) (Karabela et al., 2011) (Sato, Chiu, & Reed, 2011) (Moverare & Johansson, 2010) (Cruchley, Evans, Taylor, Hardy, & Stekovic, 2013). This is an especially sensitive application in that the surface of the disk and blade attachment points represent the most highly stressed areas of a turbine. Accordingly, crack tip oxidation has experienced in-depth attention (Kitaguchi et al., 2013) (Karabela, Zhao, Lin, Tong, & Hardy, 2013). Typical metallic aluminide and NiCrAlY coatings, engineered for higher temperature blade exposures and Type II hot corrosion resistance, actually lead to fatigue debits because of CTE mismatch stresses, lower strength, and tendency for brittle behavior in a disk environment. This warrants modified approaches, such as fully ductile Ni-Cr coatings or fatigue resistant, refractory strengthened NiCrAl-Ta, W “EQ” coating alloys (Mercer, Kawagishi, Tomimatsu, Hovis, & Pollock, 2011).

We therefore propose that Cr_2AlC may be worth considering as a potential coating in this application. It has three desirable attributes: strain tolerance due to microlaminate kinking, a relatively high CTE ($13 \times 10^{-6}/^\circ\text{C}$), and good Type I hot corrosion resistance. Our current studies indicate good Type II low temperature corrosion behavior as well. However little information is available regarding cyclic thermal stability of this coating with a superalloy. Thus the purpose of the present paper is to examine the compatibility of a hot pressed Cr_2AlC -LSHR disk alloy hybrid after repeated cycling to 800 °C. Interfacial mechanical, oxidative, and diffusional stabilities are the primary focus points.

Materials and Procedure

The alloy portion of the couple was LSHR (Low γ' Solvus temperature, High Refractory) developed by NASA for disk applications (Timothy P Gabb, Gayda, Telesman, & Kantzos, 2005). The AF-LSHR composition is:



Production scale powder metallurgy disks were produced by argon atomized, consolidated, hot compacted powders, followed by extrusion and isothermal forging. Specimen blanks were supersolvus heat treat at 1171 °C for 2 h, cooled at 72 °C/min., then aged at 855 °C/4 h and 775 °C/8 h. Phase constituents were primarily γ -Ni(Co,Cr,Mo,W) solid solution, strengthened by dense γ' -Ni(Ti,Ta,Nb)₃Al precipitates, and dispersed (Ta,Nb,Ti)C carbide, coarse (W,Mo,Cr)₃B₂ boride, and fine grain boundary (W,Cr)₂₃C₆ carbide particles. (T P Gabb & Miller, 2012).

The starting Cr₂AlC MAX phase ingot, approximately 2- by 2- by 12-cm, was obtained from Sandvik/Kanthal. As-received density was ~67% based on an assumed theoretical density of 5.22 g/cm³. Thus an effort was made to improve density by hot pressing in vacuum (77 Pa or 10⁻⁶ torr) using graphite dies. It was found that hot pressing at 1300 °C for 2 h using 35 MPa pressure resulted in 97% density. The phase constituency was estimated by XRD Reitveld analyses to be ~92.3% Cr₂AlC, 3.9% Al₂O₃, and 3.8% Cr₇C₃ which did not change appreciably in bulk with 1300 °C hot pressing, 1100 °C diffusion bonding, or 800 °C oxidation.

Coupons ~ 6- by 12-mm were sectioned from the hot pressed Cr₂AlC and LSHR using a diamond wafer saw. Thickness was ~ 0.3 and 1.8 mm, respectively. These were polished to 2400 grit SiC emery finish and vacuum hot pressed at 1100 °C for 4 h under 85 MPa pressure (DC2). Hot pressing caused substantial deformation of the LSHR alloy, to the extent that the slightly undersized Cr₂AlC layer was fully impressed into the metal. For this reason a second couple (DC3) was prepared for a subsequent 1000 h oxidation test, using 1.5 mm Cr₂AlC and only 50 MPa pressure. Only minimal deformation of the LSHR alloy was noted. Grafoil mold release was burned off at 800 °C for 1 h, and one end of the couple was sectioned for as-diffusion bonded metallography.

The cut edge and major surfaces were polished to 4000 grit emery and ultrasonically cleaned in ethanol. The couple was oxidized at 800 °C in air for 100 h in a Thermolyne resistance muffle furnace, with intermittent removal for weight change and optical photography. The materials were analyzed by conventional metallographic, X-ray diffraction (XRD), and scanning electron microscopy (SEM) techniques before and after oxidation. SEM samples were coated with a conductive carbon or Au-Pd coating. Because of fine particle sizes and carbon coating, more quantitative assessments of carbide phases and thin oxide nodules were not attempted. Vacuum infiltrated epoxy mounted and polished cross-sections were prepared before and after oxidation. An additional feature of this study was the examination of surface scales formed on the edge, which had been pre-polished to 4000 grit emery, to show microstructural evolution of the scales across the interfacial bond.

Results

The weight change behavior of the diffusion bonded hybrid couples are shown in Figure 1(a). Very little oxidation occurred, gaining only 0.09 mg/cm² after 100 h. This would be equivalent to a low parabolic rate constant of 7.23×10^{-5} mg²/cm⁴/h for the couple, although cubic kinetics may ultimately be a more accurate description of layer growth rates (Tallman et al., 2013). However, both the Cr₂AlC and LSHR alloy contribute to this value, so it is impossible to precisely characterize the weight change contribution of either. The weight change of the second couple was oxidized in a similar matter and achieved only 0.17 mg/cm² after 1000 h. There were no signs of delamination or deterioration of the bond interface. The literature suggests weight changes on the order of 0.061 and 0.20 for Cr₂AlC oxidized for 100 and 1000 h, respectively, (Z. J. Lin et al., 2007) and ~0.31 and 0.57 mg/cm² for LSHR oxidized for 100 and 1000 h, respectively. (T. P. Gabb, Sudbrack, Draper, MacKay, & Telesman, 2014). Since weight gain is not a focus of this study, the kinetics are not discussed in more detail.

XRD analyses of the oxidized surfaces is presented in Table 1. The Cr₂AlC side formed primarily α -Al₂O₃, with an increase in the Cr₇C₃ phase. Also, another Cr₃C₂ carbide depletion phase was identified. The LSHR side formed primarily an α -Cr₂O₃ scale with some (Ti,Ta,Cr)O₆ tetragonal rutile-type oxide.

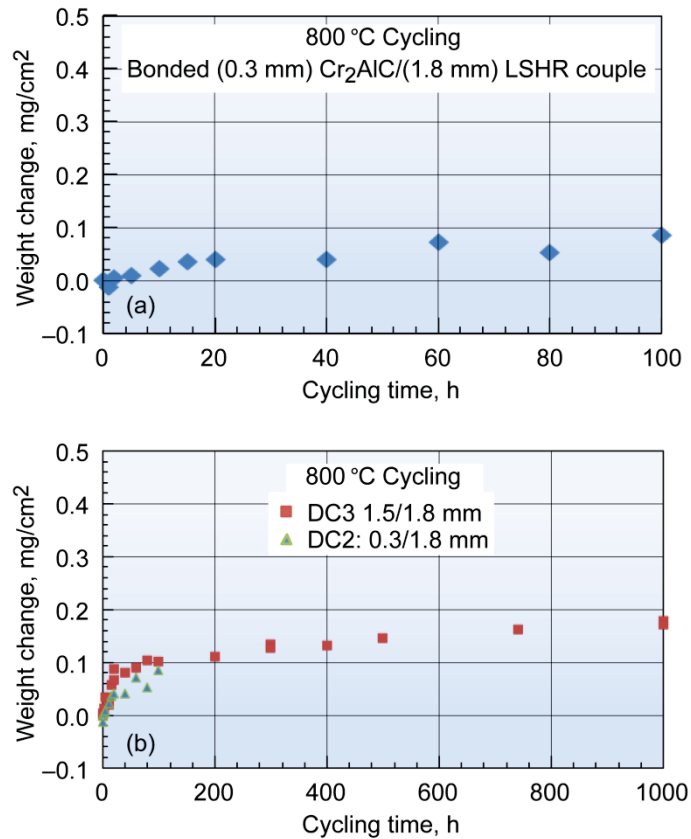


Figure 1.—Intermittent 800 °C oxidation of hybrid LSHR-Cr₂AlC diffusion couples showing stable protective behavior. (a) DC-2, 100 h: 0.3 mm Cr₂AlC/1.8 mm LSHR. (b) DC-3, 1000 h: 1.5 mm Cr₂AlC/1.8 mm LSHR.

TABLE 1.—XRD SURFACE ANALYSIS OF HYBRID COUPLE OXIDIZED 100 h AT 800 °C

MAX phase				
Chemical formula	Compound name	Crystal system	Ref. code	Relative intensity
Cr ₂ AlC	MAX phase	Hexagonal	04-007-2697	Strong
Al ₂ O ₃	α-alumina	Rhombohedral	01-089-7716	Weak
Cr ₇ C ₃	chrome carbide	Orthorhombic	01-089-5902	Strong
Cr ₃ C ₂	chrome carbide	Orthorhombic	04-004-4541	Weak
LSHR				
Chemical formula	Compound name	Crystal system	Ref. code	Relative intensity
Ni(Nb)	γ-Ni solid solution	Cubic	04-003-2243	Strong
(Ti,Ta,Cr)O ₆	rutile	Tetragonal	01-076-7954	Weak
(Cr,Ti) ₂ O ₃	α-chromia	Rhombohedral	01-082-0211	Medium

The bonded interface of the diffusion couples are presented below as comparisons of polished cross-sections of the hot pressed structure (HP) and the heat treated structure (OX), and the oxidized edge (EDGE). The cut and oxidized edge is shown in the optical micrographs of Figure 2. The full thickness of the Cr_2AlC layer can be seen to be on the order of $250\text{ }\mu\text{m}$, with an overall diffusion zone of $\sim 50\text{ }\mu\text{m}$. There is no appreciable change from 20 to 100 h of oxidation. Nor are any edge cracks or delamination visible. This indicates the relatively stable nature and low CTE mismatch stress of this couple. Optical micrographs are presented in Figure 3 for the mounted and polished samples, before (HP) and after (OX) the thermal treatment. A complex, multiphase interdiffusion zone can be seen, without major change due to the thermal exposure. Detailed SEM and energy dispersive spectroscopy (EDS) characterization is thus presented below for all three cases.

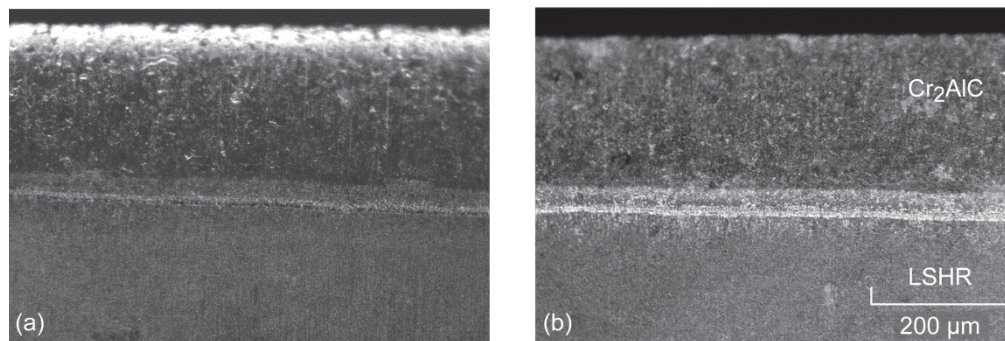


Figure 2.—Surface scales of diffusion bonded LSHR- Cr_2AlC after 800 °C oxidation. (a) 20 h. (b) 100 h. (Optical micrographs of exposed interface)

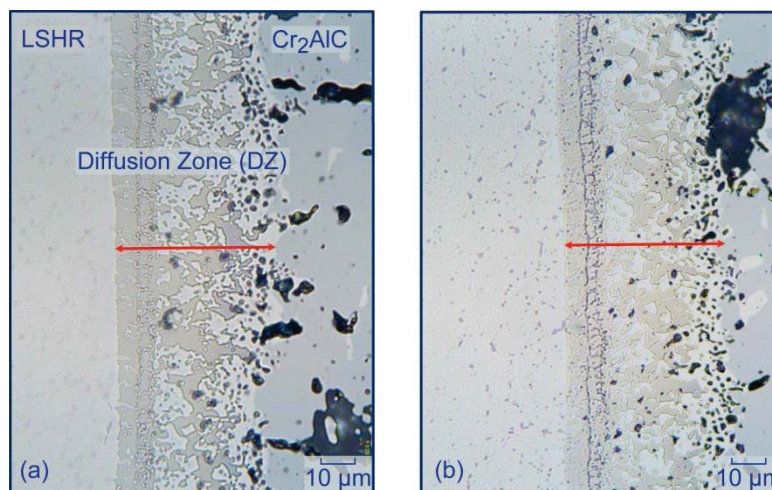


Figure 3.—Overall diffusion zones at the LSHR- Cr_2AlC interface. (a) As bonded (b) After 100 h at 800 °C. (Optical micrographs of polished cross sections)

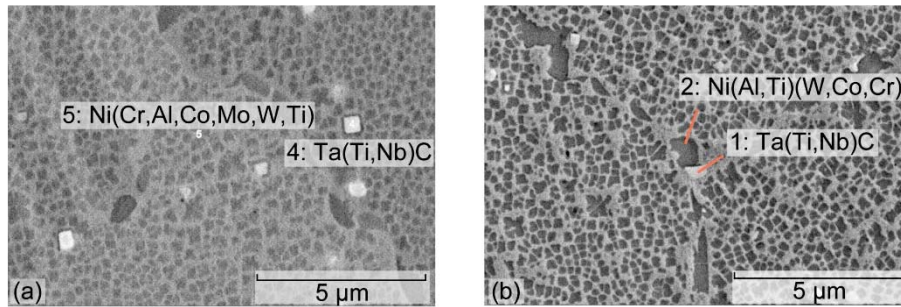


Figure 4.—Fine $\gamma'\gamma'$ and MC carbide particles in LSHR (Away From Interface (AFI)).
(a) Hot pressed. (SE) (b) After 100 h at 800 °C. (BSE)

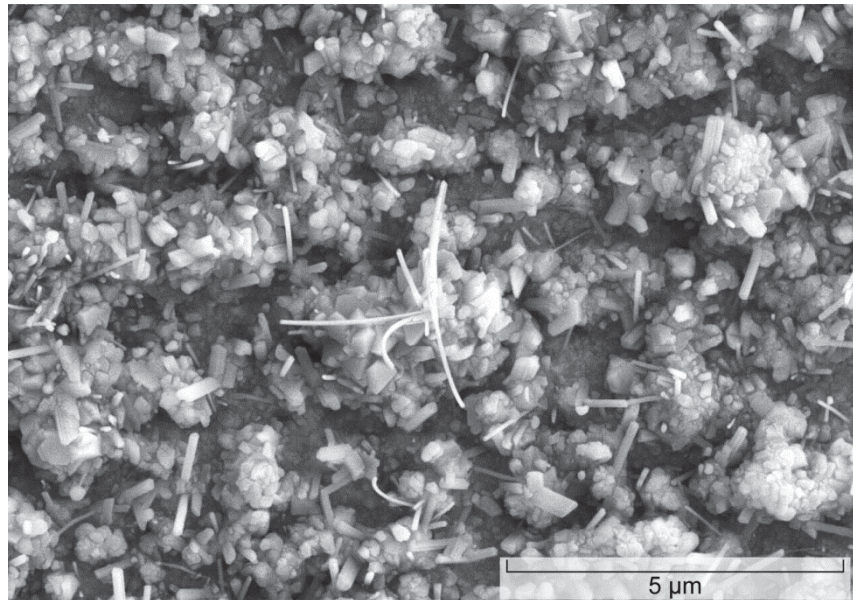


Figure 5.—Fine needles and faceted crystallites formed on LSHR (AFI) after oxidation at 800 °C for 100 h.

Away from the interface, LSHR and Cr_2AlC structures are characterized as unaffected endpoints. LSHR presented in Figure 4 shows densely populated, fine $\gamma'\text{-Ni}_3\text{Al}$ precipitates (#5,2) in both HP and OX polished samples. They are only slightly distinguished in backscattered electron (BSE) images (4) because of the atomic weight similarity to the $\gamma\text{-Ni(ss)}$ matrix, and not appreciably altered by the 800 °C, 100 h oxidation treatment. In contrast, sparsely distributed submicron $(\text{Ta,Nb,Ti})\text{C}$ carbide particles (#4,1) are easily distinguished because of their high refractory metal content. The corresponding LSHR region of the oxidized edge exhibits a profusion of Al,Cr,Ti,Ni-rich oxide nodules with faceted and needle-like surface crystals, Figure 5, with no obvious correlation with substrate microstructure. The various features characterized by EDS obtained at 15 kV are summarized in Table 2 and catalogued by feature number and exposure. Here EDS relative peak intensities are indicated in order of decreasing level, with > indicating a difference of more than 15% and >> indicating a difference of more than 50%. Representative spectra will be presented later. Thus the unaffected LSHR alloy exhibits a Ni-rich matrix with low levels of all the alloying elements (#5), while the various carbides are rich in Ti, Cr, or refractory metals (#4). The LSHR scale features were rich in Al, Cr, Ti, Ni. Except for the Al-rich scale, this was consistent with XRD analyses that identified $\text{Cr}(\text{Ti})_2\text{O}_3$ corundum patterns.

TABLE 2.—SEM/EDS FEATURE ANALYSIS AND EXPOSURE EFFECTS (COLOR CODING BY SIMILAR ITEMS). FEATURES ARRANGED FROM LSHR TO Cr₂AlC

	Point	Polished cross-sections: HP P025 As-Hot Pressed			Point	Polished cross-sections: OX P026 After Oxidation			Point	Polished sample edge: Oxidized EDGE section		
LSHR	5	matrix	Ni>>(Co,Cr,Al,W,C,Mo,Ti)	γ/γ′	1	g.b. light particle	Ta>(Ti,Nb)>C>(Cr,Ni,Co)	MC	0A	facets, needles	O>(Al,Cr)>(Ti,Ni)	Al(Cr) ₂ O ₃
LSHR	4	grey particle	Ta>(Ni,Nb,Ti)>C>(Al,Cr,Co)	MC	2	g.b. precipitate	Ni>>(Al,Ti,W,Co,Cr)	γ′				
LSHR _{DZ}	9	grey particle	Ta>(Nb,Ti)>>C	MC	6	grey particle	Ta>(Nb,Ti)>C>(Cr,Ni,Co)	MC	A	nodule needles	O>Ti>(Al,Cr)>>Ni	TiO ₂
LSHR _{DZ}					7	needle	Ni>>(Al,Cr)>(W,Mo,Ti)	TCP	B	flat base	Al>(Cr,Ni)>(Co,O)>Ti>(Ta,W)	Ni(Al,Cr) ₂ O ₄
LSHR _{DZ}					8	matrix	Ni>>Cr>(Al,Co)>Ti	γ/γ′	C	nodule needles	O>(Ti,Al,Cr)>(Ni,Co,O)>(Ta,W)	(Al,Cr)TiO ₄
DZ _{LSHR}	6	white particle	W>>(Mo,Cr)>(Ti,C)	M ₃ B ₂	5	D.Z. matrix	(Ni,Al)>>>(Co,Cr,Ti)	β-NiAl	G	nodule	O>Cr>Ti>(Ta,Al)	CrTiO ₄
DZ _{LSHR}	7	grey particle	Ta>(Ti,Nb)>>(Ni,Al,C)	MC	3	white particle	W>(Mo,Cr)>C	M ₃ B ₂	H	faceted nodule	O>(Al,Cr,Ti)>>(Ni,Co)	(Al,Cr) ₂ O ₃ -CrTiO ₄
DZ _{LSHR}	8	underlayer	Ni>Al>>(Cr,Co,Ti)	β-NiAl	4	grey particle	Ni>Al>(Cr,Co)>(W,Mo,Ti)	γ′	D	flat base	Al>O>(Cr,Ni,Co)>(Ti,Ta,W)	
DZ1 _{Cr₂AlC}	13	dark particle	Al>>O>(Ni,Ti,Cr,Co)	Al ₂ O ₃	9	dark bond line particle	Al>>O>(Ti,Ta,Nb,Cr,Co)	Al ₂ O ₃	E	flat layer	Al>>(O,Cr,Ni)>(Co,Ti,Ta,W)	Al ₂ O ₃
DZ1 _{Cr₂AlC}	12	light phase	(Ta,Ti)>(Al,Nb)>(Ni,C)	MC	11	light phase	(Ta,Ti)>(Al,Nb)>(Ni,C)>Cr,Co	MC	F	smooth nodule	(Al,O)>Cr>Ti>(Ni,Co)>(W,Ta)	(Al,Cr,Ti) ₂ O ₃
DZ1 _{Cr₂AlC}	11	underlayer	Ni>Al (Cr,Co)	γ/γ′	10	grey particle	Ti>W>Nb>Mo>(C,Al)>>(Ni,Co,Cr)	MC	I	sea urchin	Al>O>Ti>Cr>(Ni,Co,W,Ta)	Al ₂ O ₃
DZ2 _{Cr₂AlC}	10	amorphous islands	Cr>>(W,Mo)>C	Cr ₇ C ₃	14	underlayer	Ni>>Al>>(Ti,Cr,Co)>(W,Mo)	γ/γ′	J	amorphie fingers	Al>O>Cr>(Ni,Co)	Al ₂ O ₃
DZ2 _{Cr₂AlC}					15	between carbide network	(Ni,Al)>>(Cr,Co)	β-NiAl	K	granular islands	(Cr,O)>Al>(Ni,Co)	Cr ₂ O ₃
DZ2 _{Cr₂AlC}					12	amorphous islands	Cr>(W,Mo)>C	Cr ₇ C ₃	M	amorphie fingers	Al>O>Cr>(Ni,Co)	Al ₂ O ₃
DZ2 _{Cr₂AlC}					13	dark particle	Al>>O	Al ₂ O ₃	L	granular islands	(Cr,O)>>Al	Cr ₂ O ₃
DZ2 _{Cr₂AlC}					16	outer D.Z. matrix	(Ni,Al)>>(Co,Cr)	β-NiAl	N	smooth transition	Al>O>>Cr>(Ni,Co)	Al ₂ O ₃
DZ2 _{Cr₂AlC}					17	amorphous islands	Cr>C>Al	Cr ₇ C ₃				
Cr ₂ AlC	1	light phase	Cr>>C	Cr ₇ C ₃	18	light phase	Cr>>C	Cr ₇ C ₃	Q	granular	Cr>O	Cr ₂ O ₃
Cr ₂ AlC	2	dark particle	Al>>O	Al ₂ O ₃	19	dark particle	Al>>O	Al ₂ O ₃	O	dark particle	Al>>O	Al ₂ O ₃
Cr ₂ AlC	3	matrix	Cr=Al>>C	Cr ₂ AlC	20	matrix	(Cr,Al)>>C	Cr ₂ AlC	P	smooth matrix	Al>(Cr,O)	Al(Cr) ₂ O ₃

For the HP sample away from the interface at the other extreme, the Cr_2AlC layer can be seen in Figure 6 as the three-phase material previously indicated. The matrix phase here is Cr_2AlC (#3), the light phase particles are Cr_7C_3 (#1), and the dark particles are Al_2O_3 (#2), consistent with the associated EDS peak intensities catalogued in Table 2. The matrix phase on the sample edge was oxidized to an $\text{Al}(\text{Cr})_2\text{O}_3$ lenticular scale structure, Figure 7(a), similar to that reported previously for 900 °C oxidation. (D.B. Lee et al., 2007). However, a coarser Cr_2O_3 granular scale was observed in local areas probably corresponding to and growing on the Cr_7C_3 impurity particles, Figure 7(b). The more open structure here may be a result of CO/CO_2 gas evolution occurring during oxidation.

The as-hot pressed polished cross-section (HP) in Figure 8(a) shows ~260 μm thick Cr_2AlC layer remaining after removing 40 μm during surface preparation and a primary diffusion layer of ~47 μm . More subtle gradients beyond this primary zone can also be distinguished. The as-hot pressed cross-section is compared to that after thermal exposure (8c, OX) and to the oxidized edge (8b, EDGE). The primary $\text{NiAl} + \text{Cr}_7\text{C}_3$ diffusion zone appears to have grown by an additional 4 to 5 μm . Thicknesses of the various diffusion zones characterized below are summarized in Table 3.

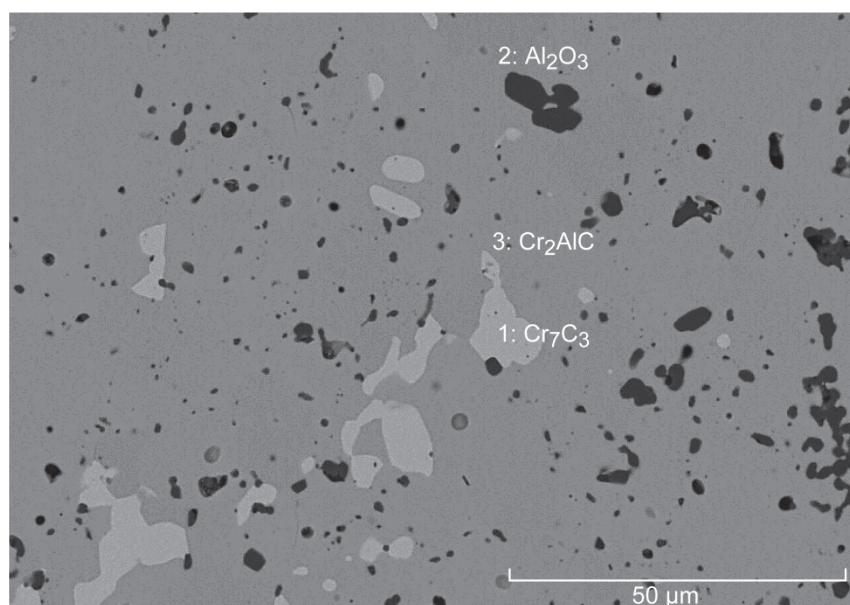


Figure 6.— Cr_7C_3 and Al_2O_3 particulate phases in Cr_2AlC (AFI). (BSE)

TABLE 3.—DIFFUSION LAYER THICKNESSES (μm)

	LSHR carbide growth	LSHR Ni-Al	Cr_2AlC Ni-Al	Cr_2AlC carbide growth	ΔDZ
Polished hot pressed HP	81.0	5.8	5.4	39.3	----
Polished oxidized OX	77.7	7.2	6.8	42.6	+4.7
As-oxidized EDGE	(22.8)	6.4	6.5	41.1	+2.4

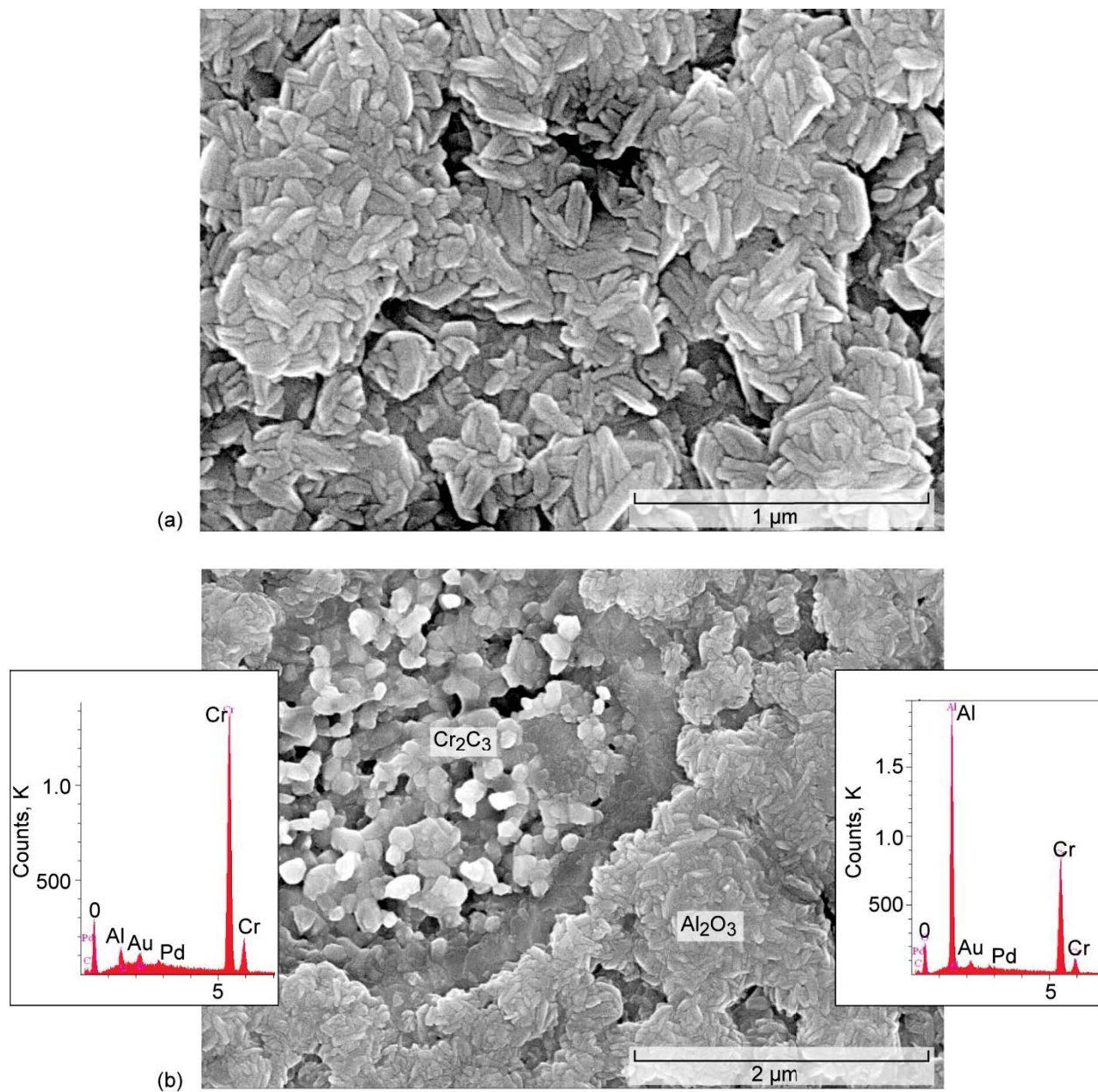


Figure 7.—Microstructure of scale formed on Cr_2AlC (AFI) after oxidation at 800 °C for 100 h. (a) Matrix of fine transition Al_2O_3 lenticular platelets. (b) Local area of angular Cr_2O_3 crystallites.

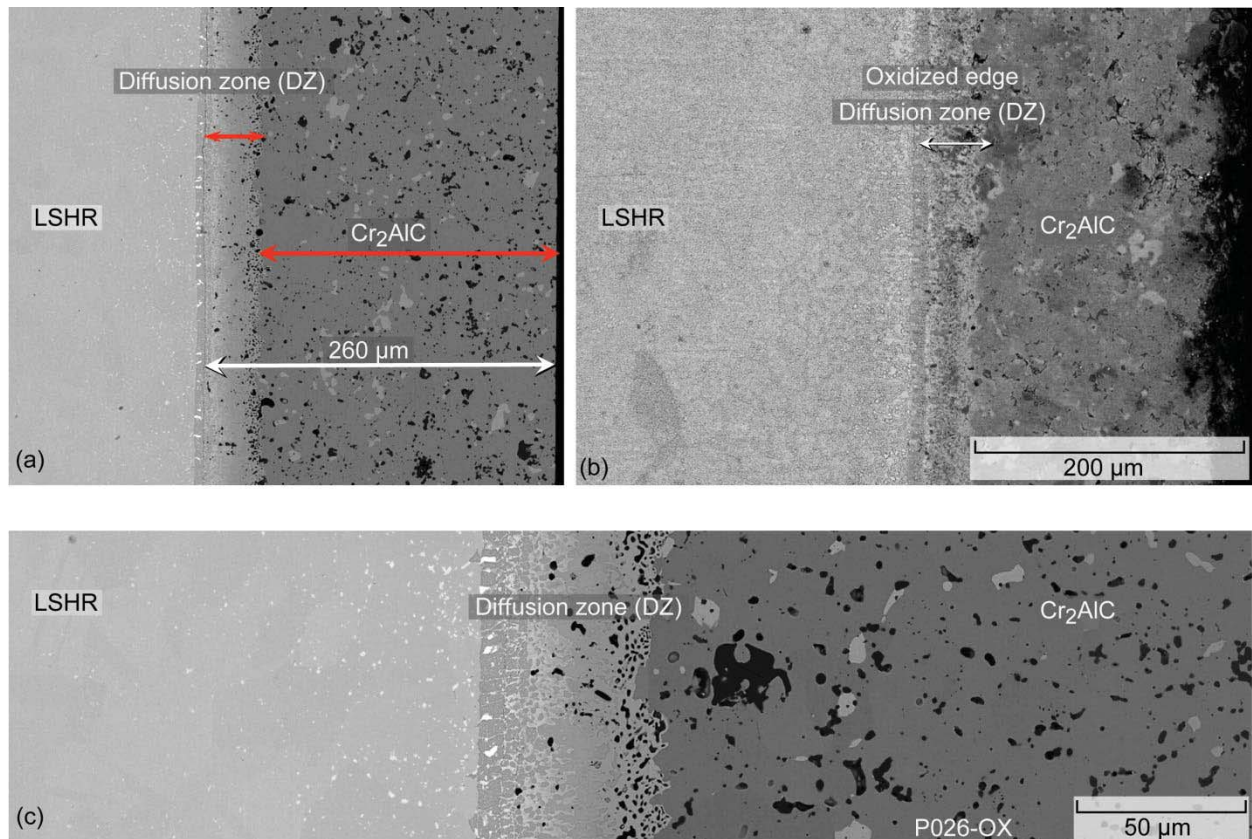


Figure 8.—Overview of diffusion bonded LSHR-Cr₂AlC couple interface showing corresponding regions after oxidation. (a) Polished cross section, as hot pressed. (b) Polished sample edge, after oxidation at 800 °C for 100 h. (c) Polished cross section after 100 h at 800 °C.

Interfacial details are further compared in Figures 9 to 11 with EDS descriptions of labeled specific features listed in Table 2. On the LSHR alloy side (left) for the as-hot pressed interface (HP), Ta(Ti,Nb) rich carbides (#9,7) are observed in both the Ni-rich alloy matrix (#5) and in the NiAl primary diffusion zone (#8), Figure 9. Larger, bright W-rich borides (#6) are also in this region. The original bond line (B.L.) is indicated by the dashed yellow line, decorated by the fine dark Al₂O₃ precipitates (#13). Moving toward the Cr₂AlC layer, light (Ta,Ti)C carbides (#12) are again seen in an NiAl matrix (#11). Moving further right, a high volume percent of a light amorphous Cr-rich phase is present, probably a diffusional growth of the Cr₇C₃ impurity phase. This phase is well known to be a sublayer diffusion zone that grows under the alumina scale as Al is extracted from Cr₂AlC during oxidation. (D.B. Lee et al., 2007)(Z. J. Lin et al., 2007). Also, it has been predicted thermodynamically and shown experimentally that NiAl will deplete Al from Cr₂AlC to form Cr₇C₃ (Hajas, et al. 2010). Given that the high content of Al in Cr₂AlC is likely to diffuse into the Ni-based LSHR alloy, Cr₇C₃ might also be expected as a depletion zone in an LSHR- Cr₂AlC couple.

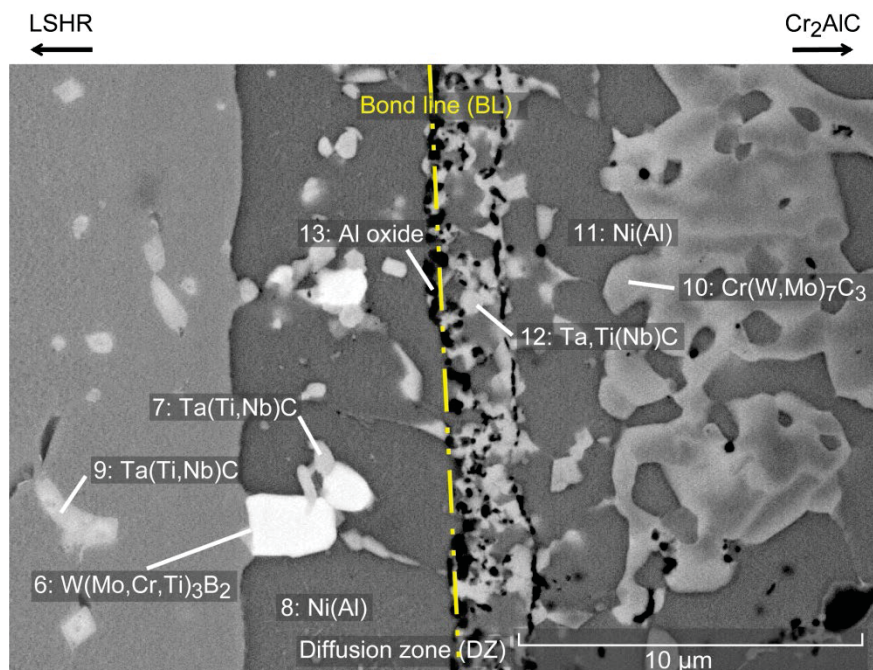


Figure 9.—Interface detail for hot pressed cross section of LSHR-Cr₂AlC couple. Ni-Al diffusion zone (8,11) with MC (7, 9, 12), M₃B₂ (6), and Cr₇C₃ (10) precipitates and Al₂O₃ (13) bond line stringers. (BSE)

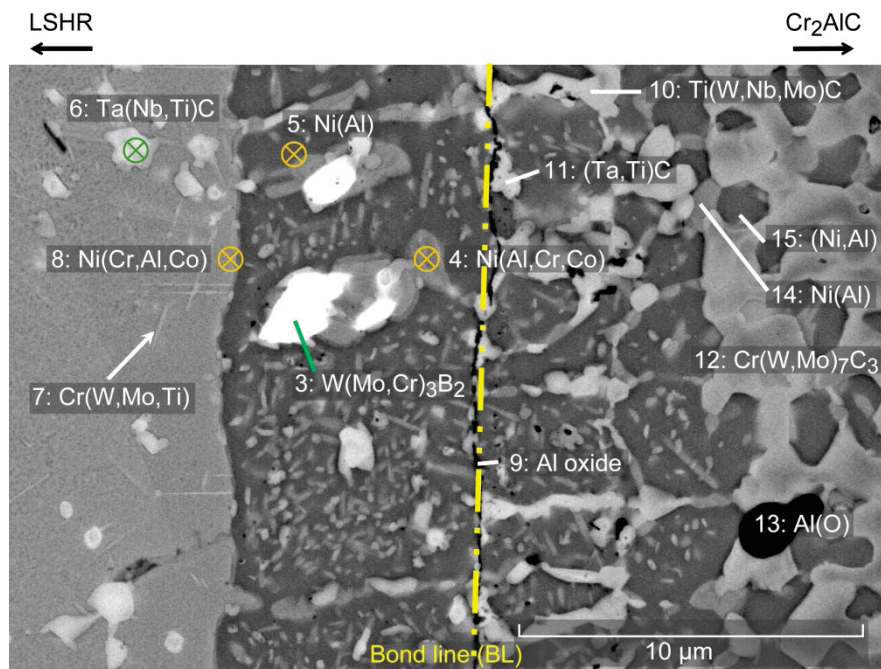


Figure 10.—Interface detail for polished cross section of oxidized LSHR-Cr₂AlC couple. Growth of Ni-Al diffusion zone (5, 15) with MC (6, 10, 11), M₃B₂ (3), and Cr₇C₃ (12) precipitates and Al₂O₃ (9) bond line stringers. γ (4, 14) and similar Widmanstätten in Ni-Al zones and TCP plates in LSHR are also evident. (BSE)

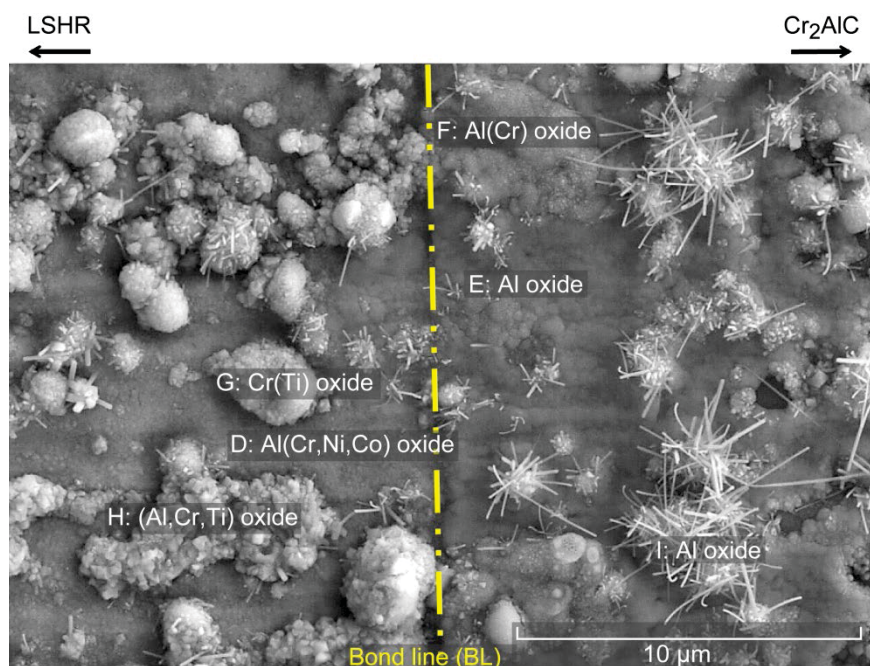


Figure 11.—Interface detail for oxidized edge of LSHR-Cr₂AlC couple. Smooth, planar Al-rich oxide (D, E, F) and Al₂O₃ whiskers (I) over both Ni-Al diffusion zones. Faceted nodules with Cr and Ti (G, H). Bond line Al₂O₃ no longer distinctly apparent.

Figure 10 shows the interfacial details after oxidation in a mounted and polished cross section (OX). Features similar to those before oxidation are identified: Ta(Ti,Nb) MC carbides in LSHR (#6,11), Ni-Al primary diffusion zone (#5), bright W-rich borides (#3), fine Al₂O₃ precipitates (#9), and amorphous Cr₇C₃ colonies (#12). Some additional features are now apparent. A Cr(W,Mo,Ti)-rich acicular phase (#7) is present in the LSHR side, probably σ . And a weakly Widmanstätten Ni-Al precipitate (#4,14) appeared in the Ni-Al primary diffusion zone (#5,15). Semi-quantitative analysis of the primary diffusion zone yielded Ni-13Co-38Al, consistent with hypostoichiometric β -NiAl. A grey carbide particle near the LSHR interface was estimated as 37Ti-17Ta-26Nb (carbon excluded from analysis). The fine $\leq 0.5 \mu\text{m}$ precipitates in the NiAl matrix varied considerably, with typical estimates near 30Ni-20Co-20Al-20Cr-3Ti, but not immediately suggestive of any common alloy phase.

Scale features of this interface area in the exposed edge are presented in Figure 11. Although a planar boundary can be discerned, there is no sign of bond line degradation. The fine particles at the bond line (B.L.) and many of the dark Al₂O₃ precipitates appear to have been masked by the scale features, while other structural variations and gradients remain. In general, flat Al-rich oxide (#D,E) formed over the NiAl diffusion zone with numerous nodule-type structures. On the LSHR side, the nodules (#G,H) were more often enriched in Cr, Ti, while on the Cr₂AlC side, they were primarily Al-rich (#F,I). Figure 12 presents a high magnification image of the Al-oxide needle colony (#I) present in Figure 11. While some rounding is apparent at the needle tips, spherical balls associated with a VLS process were not present at the ends. Figure 13(a) presents the interlocking structures of the Ni-Al matrix (#16) and large area fraction of the Cr-carbide (#17) within the diffusion zone produced by hot pressing. Figures 13(b) and (c) are from the oxidized edge, showing smooth Al-rich (#J,M,N) and granular Cr-rich oxide (#K,L), respectively, formed on these phases near the middle (13b) and Cr₂AlC region (13c,d) of the diffusion zone.

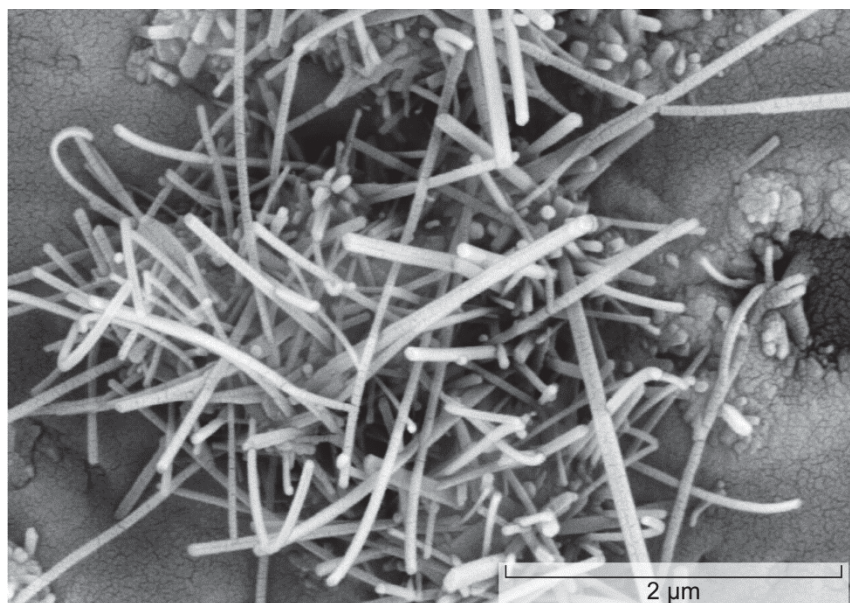


Figure 12.—Cluster of Al_2O_3 whiskers over Cr_2AlC side of inner diffusion zone. (BSE)

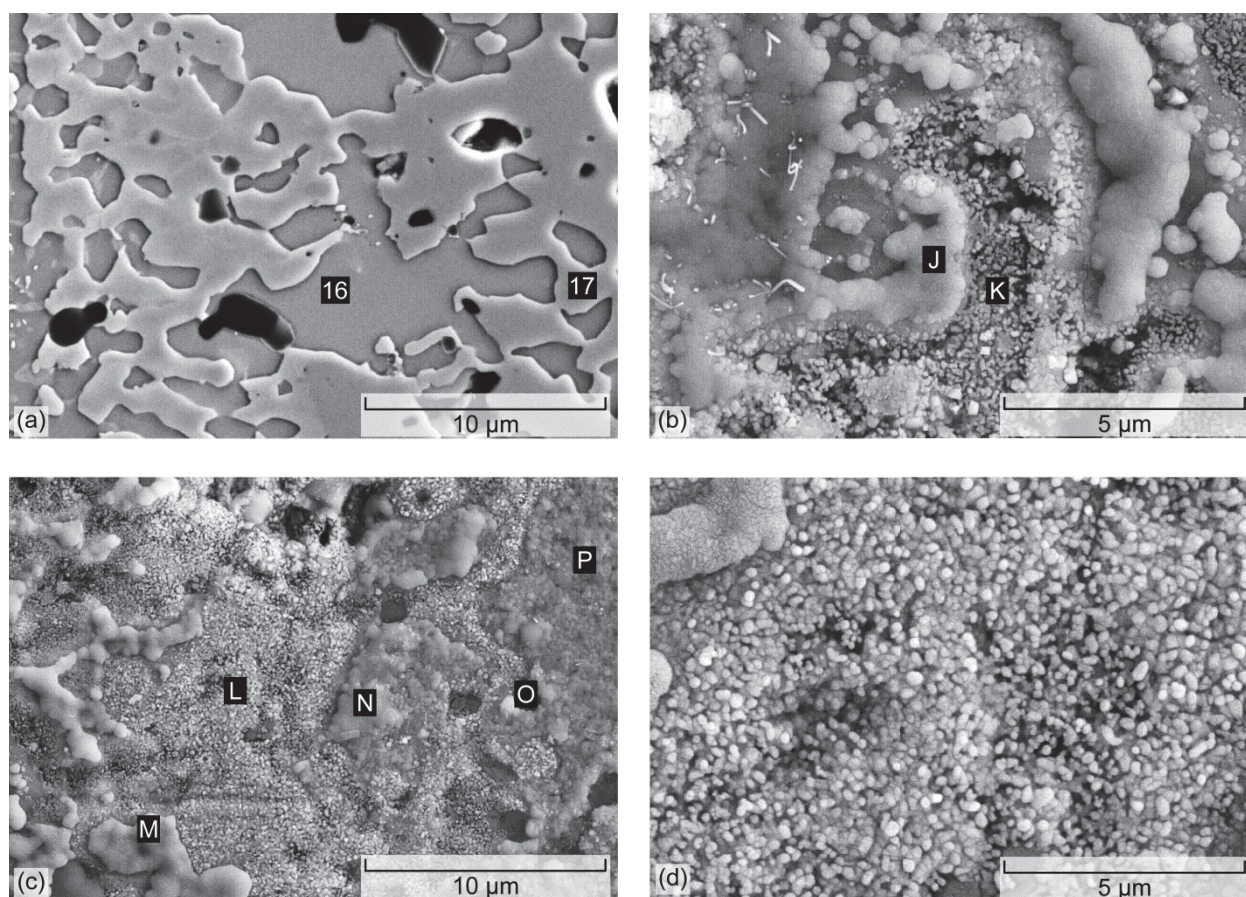


Figure 13.—Features related to the Cr_2AlC end of the diffusion zone. (a) Interlocking amorphous islands of Cr_7C_3 (17) and fingers of Ni-Al matrix (16) near Cr_2AlC layer after hot pressing. (b) Smooth Al-rich (J) and porous angular Cr-rich crystallites (K) formed over structure in (a) after oxidation. (c) Transition from granular structures in (b) to smooth Al_2O_3 scale (M, N, P) formed over the Cr_2AlC phase.

Representative EDS spectra are compared for the HP, OX, and EDGE samples in Figures 14 to 16 for the unaffected LSHR layer, the Ni-Al diffusion zone matrix phase, and the Cr-carbide phase near the Cr_2AlC layer, respectively. Strong Al, Cr, and Ti enrichments are seen in the oxidized LSHR surface (Figure 14(c)), as compared to Ni-rich polished cross-sections (Figures 14(a) and (b)). Little change occurred in the Ni-Al diffusion zone after oxidation (Figures 15(a) and (b)), but the scale formed on this phase was very Al-rich, with only some Cr. Finally, the Cr-rich carbide phase in the diffusion zone changed little and oxidized to the Cr(Al)-rich oxide, Figure 16, interestingly without any Al evident in the starting phase.

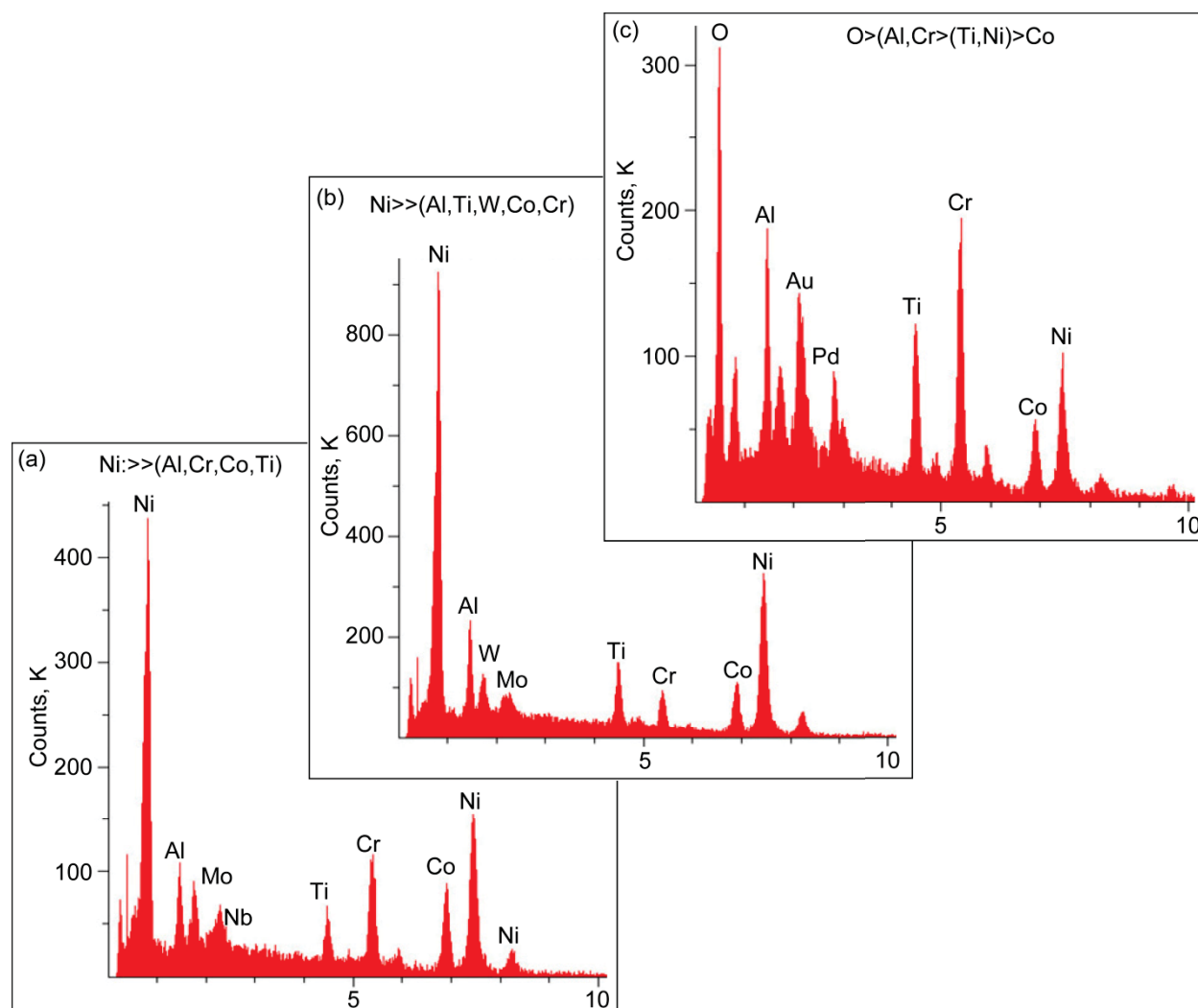


Figure 14.—EDS spectra of LSHR alloy region. (a) Ni-rich matrix (5, Figure 4a) in hot-pressed sample. (b) Ni-rich matrix in oxidized sample. (c) Oxidized edge showing Al, Cr, Ti, Ni-rich scale (Figure 5) over LSHR side of couple.

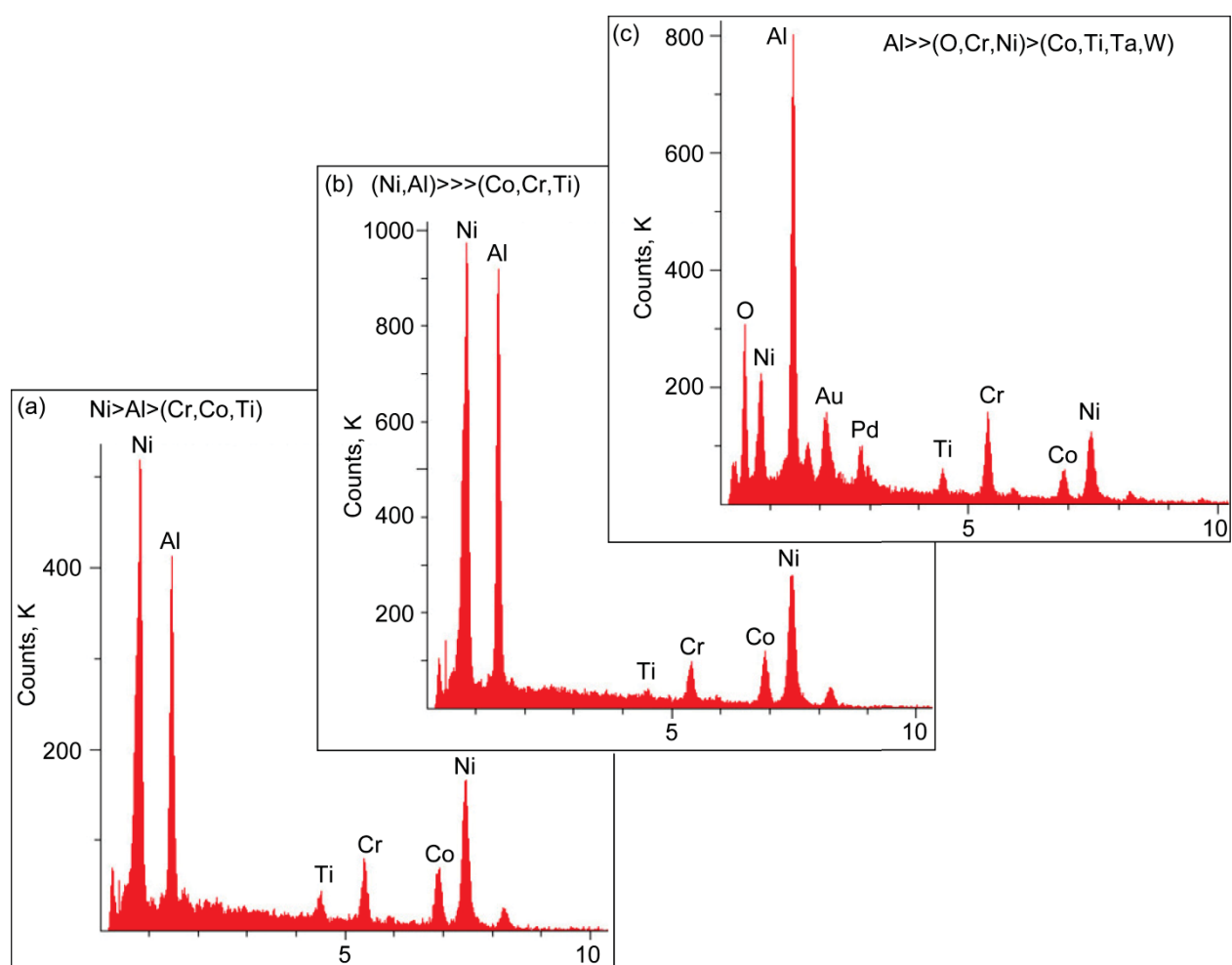


Figure 15.—EDS spectra of diffusion zone matrix phase. (a) Ni-Al rich matrix (8, Figure 9) in hot-pressed sample. (b) Ni-Al rich matrix (5, Figure 10) in oxidized sample. (c) Oxidized edge showing Al-rich (Cr,Ni) scale (E, Figure 11) over Ni-Al diffusion zone phase.

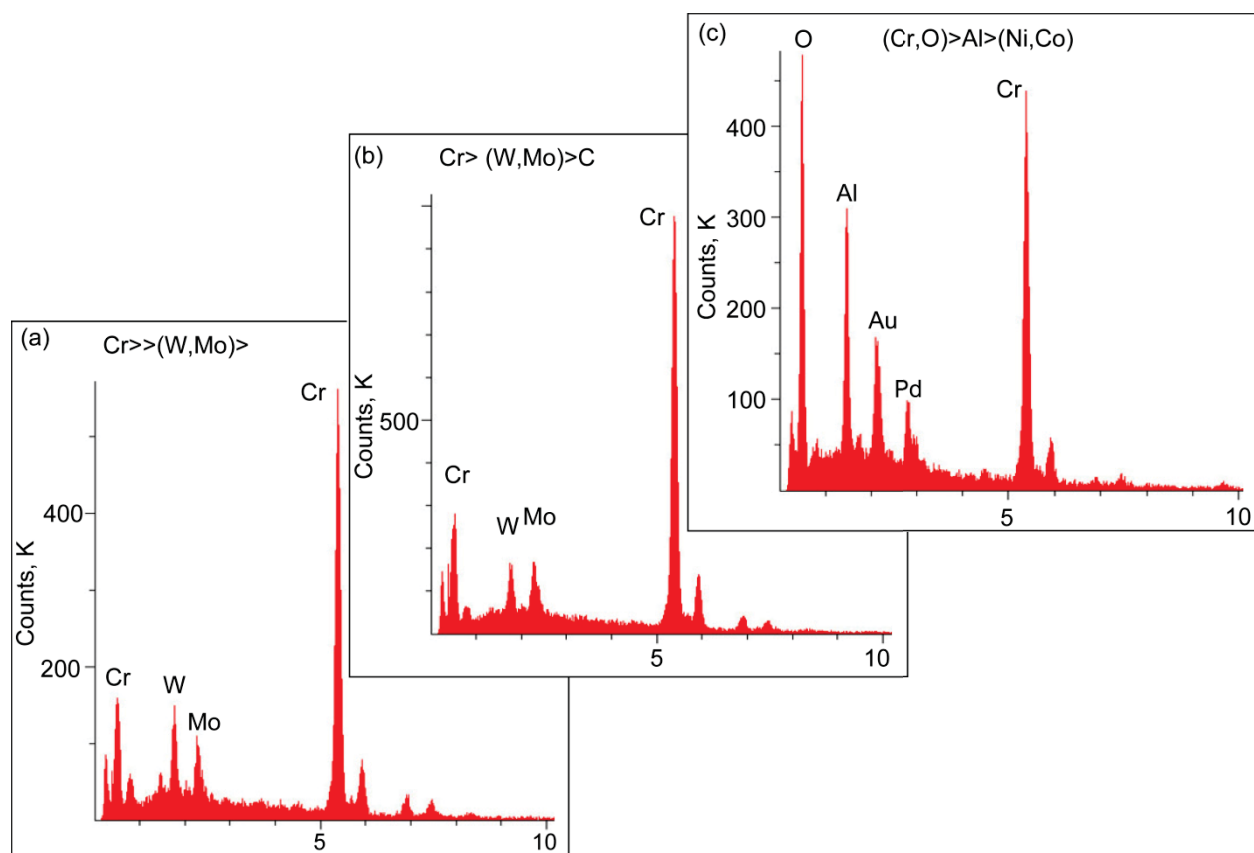


Figure 16.—EDS spectra of amorphous network carbide in outer Cr_2AlC diffusion zone. (a) Cr-rich (W,Mo) islands (10, Figure 9) in hot-pressed sample. (b) Cr-rich (W,Mo) islands (12, Figure 10) in oxidized sample. (c) Oxidized edge showing Cr,Al-rich scale (K, Figure 13) over Cr_7C_3 diffusion zone phase.

Discussion

Thus a dense wafer of Cr_2AlC has been successfully bonded to an advanced disk alloy, LSHR, at 1100°C . A noticeable amount of interdiffusion took place, producing a distinct interface layer of an Ni-Al rich zone, presumably $\beta\text{-NiAl}$. This zone appeared to straddle the original interface, as demarked by alumina stringers. Little growth took place after 100 h exposure to 800°C ambient air. No evidence of interfacial damage or cracking was apparent. Various modifications of the interface zone were manifested as (Ta,Ti,Nb)C carbide particles and a profusion of (Ni,Co,Al,Cr)-rich Widmanstätten precipitates. Further in toward the Cr_2AlC portion, a multiphase zone comprised of a large component of Cr-carbide has formed, analogous to the Cr_7C_3 depletion phase widely observed under alumina scales. The LSHR portion exhibited a dispersion of a σ TCP needles, with a broad, fading zone of enlarged MC carbides.

The characterization of the oxidized exposed edge reveals the most direct effect of the NiAl and Cr_7C_3 zones on oxide scale formation. That is, a relatively flat, featureless $\text{Al}(\text{Cr})_2\text{O}_3$ scale formed over NiAl, albeit with occasional nodules of distinctive, rod-like needles, while an open, granular Cr_2O_3 scale formed over the Cr_7C_3 . Unaffected regions away from the bond line exhibited similar granular Cr_2O_3 portions, presumably over the Cr_7C_3 impurity phases, with a very fine grain lenticular Al_2O_3 for the majority and remainder of the surface. On the LSHR side, the scale morphology was primarily nodular, having high Al, Cr levels.

No evidence of interfacial damage or cracking was apparent, either at the exposed surfaces or polished cross-sections. A simple bilayer stress balance equation can be used to estimate the stress in the diffusion couple (Zhu & Miller, 1996):

$$\sigma_c = \frac{(\alpha_s - \alpha_c)\Delta T E_c E_s t_s}{E_s t_s (1 - \nu_c) - E_c t_c (1 - \nu_s)}$$

where the subscripts *s* and *c* refer to substrate (LSHR) and coating (Cr₂AlC), respectively, and the other symbols, σ , α , T , E , t , refer to stress, thermal expansion, temperature, Young's modulus, and thickness, respectively. Using published values for these variables, the residual stress in the Cr₂AlC can be calculated for cooling to 25 °C, assuming a stress free temperature at 800 °C, no edge effects and no bending. This stress was found to be 520 and 340 MPa, respectively, for the 0.3 and 1.5 mm Cr₂AlC layers bonded to 1.8 mm of the LSHR alloy. This is compared to a flexural strength of 483 MPa measured for Cr₂AlC (Wu-bian Tian, Wang, Zhang, Kan, & Li, 2007) and to multi-GPa levels predicted and measured for alumina scales on MCrAl alloys. (Lipkin & Clarke, 1996) (Tolpygo, Dryden, & Clarke, 1998) This indicates that some yielding may be expected for thin Cr₂AlC layers bonded to a superalloy, but would not approach the strain energy that induces spalling of alumina scales formed on Ni-alloys, albeit upon cooling from 1100 or 1200 °C. The oxidized edge exhibited no anomalous oxidation or synergistic degrading factor. The longer 1000 h test (17 cycles), using a 1.5 mm thick Cr₂AlC wafer, appears to follow the same promising trend.

Concluding Remarks

Cr₂AlC MAX phase is relatively stable with Ni-base superalloys in 800 °C cycling and may offer promise as a high temperature, strain tolerant, corrosion resistant coating. The mechanical stability exhibited here is at least an initial indication of a promising system. The use of 0.3 or 1.5 mm thick layers in a diffusion couple indicate a robustness not normally achieved for other oxidation-resistant coatings, which are generally limited to ~ 0.1 mm or less. Most of the interdiffusion resulted from hot pressing at 1100 °C, with little growth observed at the expected 800 °C expected maximum service temperature. The ability of MAX phases to deform without cracking may provide some fatigue benefit as a coating. However the (brittle) NiAl diffusion zone may limit this benefit by its known fatigue debit as a coating for superalloys. The occurrence of some σ -phase in the LSHR side is another cause of concern. It is not clear whether an interfacial region of fine alumina stringers is an artifact of the known Al₂O₃ impurity phase in the as-received Cr₂AlC or a troublesome indigenous result of interdiffusion. In general, it is believed that lower processing temperatures will greatly decrease any detrimental diffusion effects.

Oxidation of Cr₂AlC is extremely slow at 800 °C and should pose no problem for surface degradation. As a carbide, oxygen diffusion through the MAX phase coating and oxygen-induced gas phase embrittlement (GPE) of the underlying alloy ought to be eliminated. As an alumina/chromia former with no Ni or Co exposed to the environment, Type II low temperature hot corrosion triggered by Ni-Co-Na sulfate eutectics, is also expected to be minimal for Cr₂AlC.

Future Work

It is recognized that numerous issues remain. Adequate Type II hot corrosion resistance must be fully demonstrated on bulk Cr₂AlC. Quality coatings must be produced with good corrosion resistance and good diffusional phase stability, with no debit on fatigue life. In that regard, detrimental effects of the NiAl reaction zone, Cr₇C₃ depletion zone, and σ formation must be evaluated in greater detail.

References

- Barsoum, M. W., & El-Raghy, T. (2001). The MAX Phases : Unique New Carbide and Nitride Materials. *American Scientist*, 89 (July-August), 334–343.
- Birbilis, N., & Buchheit, R. G. (2008). Measurement and Discussion of Low-Temperature Hot Corrosion Damage Accumulation upon Nickel-Based Superalloy Rene 104. *Metallurgical and Materials Transactions A*, 39 (13), 3224–3232. doi:10.1007/s11661-008-9662-7
- Cruchley, S., Evans, H. E., Taylor, M. P., Hardy, M. C., & Stekovic, S. (2013). Chromia layer growth on a Ni-based superalloy: Sub-parabolic kinetics and the role of titanium. *Corrosion Science*, 75, 58–66. doi:10.1016/j.corsci.2013.05.016
- Eklund, P., Beckers, M., Jansson, U., Högborg, H., & Hultman, L. (2010). The $M_{n+1}AX_n$ phases: Materials science and thin-film processing. *Thin Solid Films*, 518(8), 1851–1878. doi:10.1016/j.tsf.2009.07.184
- Encinas-Oropesa, A., Drew, G. L., Hardy, M. C., Leggett, A. J., Nicholls, J. R., & Simms, N. J. (2008). Effects of Oxidation and Hot Corrosion in a Nickel Disc Alloy. *Superalloys 2008 (Eleventh International Symposium)*, 609–618. doi:10.7449/2008/Superalloys_2008_609_618
- Gabb, T. P., Gayda, J., Telesman, J., & Kantzos, P. T. (2005). Thermal and Mechanical Property Characterization of the Advanced Disk Alloy LSHR. NASA/TM—2005-213645, (June), 1–75.
- Gabb, T. P., & Miller, D. R. (2012). Formation of Minor Phases in a Nickel-Based Disk Superalloy. NASA/TM—2012-217604, (July), 1–31.
- Gabb, T. P., Sudbrack, C. K., Draper, S. L., MacKay, R. A., & Telesman, J. (2014). Effects of Long Term Exposures on Fatigue of PM Disk Superalloys. *Materials Performance and Characterization*, 3(2), 1–24. doi:10.1520/MPC20130037
- Gulbiski, W. (2004). Ti-Si-C sputter deposited thin film coatings. *Surface and Coatings Technology*, 180-181, 341–346. doi:10.1016/j.surfcoat.2003.10.084
- Hajas, D. E., to Baben, M., Hallstedt, B., Iskandar, R., Mayer, J., & Schneider, J. M. (2011). Oxidation of Cr_2AlC coatings in the temperature range of 1230 to 1410 °C. *Surface and Coatings Technology*, 206(4), 591–598. doi:10.1016/j.surfcoat.2011.03.086
- Karabela, A., Zhao, L. G., Lin, B., Tong, J., & Hardy, M. C. (2013). Oxygen diffusion and crack growth for a nickel-based superalloy under fatigue-oxidation conditions. *Materials Science and Engineering: A*, 567, 46–57. doi:10.1016/j.msea.2012.12.088
- Karabela, A., Zhao, L. G., Tong, J., Simms, N. J., Nicholls, J. R., & Hardy, M. C. (2011). Effects of cyclic stress and temperature on oxidation damage of a nickel-based superalloy. *Materials Science and Engineering: A*, 528(19-20), 6194–6202. doi:10.1016/j.msea.2011.04.029
- Kitaguchi, H. S., Li, H. Y., Evans, H. E., Ding, R. G., Jones, I. P., Baxter, G., & Bowen, P. (2013). Oxidation ahead of a crack tip in an advanced Ni-based superalloy. *Acta Materialia*, 61(6), 1968–1981. doi:10.1016/j.actamat.2012.12.017
- Lee, D. B., Nguyen, T. D., Han, J. H., & Park, S. W. (2007). Oxidation of Cr_2AlC at 1300°C in air. *Corrosion Science*, 49(10), 3926–3934. doi:10.1016/j.corsci.2007.03.044
- Lee, D. B., Nguyen, T. D., & Park, S. W. (2011). Corrosion of Cr_2AlC in Ar/1%SO₂ Gas Between 900 and 1200 °C. *Oxidation of Metals*, 75(5-6), 313–323. doi:10.1007/s11085-011-9233-y
- Lee, D. B., & Park, S. W. (2011). Corrosion of Ti_3AlC_2 at 800–1100°C in Ar–0.2% SO₂ gas atmosphere. *Corrosion Science*, 53(8), 2645–2650. doi:10.1016/j.corsci.2011.05.001
- Li, J. J., Li, M. S., Xiang, H. M., Lu, X. P., & Zhou, Y. C. (2011). Short-term oxidation resistance and degradation of Cr_2AlC coating on M38G superalloy at 900–1100°C. *Corrosion Science*, 53(11), 3813–3820. doi:10.1016/j.corsci.2011.07.032
- Lin, Z. J., Li, M. S., Wang, J. Y., & Zhou, Y. C. (2007). High-temperature oxidation and hot corrosion of Cr_2AlC . *Acta Materialia*, 55(18), 6182–6191. doi:10.1016/j.actamat.2007.07.024
- Lin, Z., Zhou, Y., Li, M., & Wang, J. (2006a). Hot corrosion and protection of Ti_2AlC against Na₂SO₄ salt in air. *Journal of the European Ceramic Society*, 26(16), 3871–3879. doi:10.1016/j.jeurceramsoc.2005.12.004

- Lin, Z., Zhou, Y., Li, M., & Wang, J. (2006b). Improving the Na_2SO_4 -induced corrosion resistance of Ti_3AlC_2 by pre-oxidation in air. *Corrosion Science*, 48(10), 3271–3280. doi:10.1016/j.corsci.2005.11.005
- Lipkin, D. M., & Clarke, D. R. (1996). Measurement of the stress in oxide scales formed by oxidation of alumina-forming alloys. *Oxidation of Metals*, 45, 267–280. doi:10.1007/BF01046985
- Mercer, C., Kawagishi, K., Tomimatsu, T., Hovis, D., & Pollock, T. M. (2011). A comparative investigation of oxide formation on EQ (Equilibrium) and NiCoCrAlY bond coats under stepped thermal cycling. *Surface and Coatings Technology*, 205, 3066–3072. doi:10.1016/j.surfcoat.2010.11.026
- Moverare, J. J., & Johansson, S. (2010). Damage mechanisms of a high-Cr single crystal superalloy during thermomechanical fatigue. *Materials Science and Engineering: A*, 527(3), 553–558. doi:10.1016/j.msea.2009.08.023
- Sato, A., Chiu, Y.-L., & Reed, R. C. (2011). Oxidation of nickel-based single-crystal superalloys for industrial gas turbine applications. *Acta Materialia*, 59(1), 225–240. doi:10.1016/j.actamat.2010.09.027
- Sudbrack, C., Draper, S., Gorman, T., Telesman, J., Gabb, T., & Hull, D. (2012). Oxidation and the Effects of High Temperature Exposures on Notched Fatigue Life of an Advanced Powder Metallurgy Disk Superalloy. In J. T. E. Huron, R. Reed, M. Mills, R. Montero, P. Portella (Ed.), *Superalloys 2012: 12th International Symposium on Superalloys* (pp. 863–872). Seven Springs PA: TMS, Warrendale, PA.
- Sumner, J., Encinas-Oropesa, A., Simms, N. J., & Oakey, J. E. (2011). High temperature oxidation and corrosion of gas turbine component materials in burner rig exposures. *Materials at High Temperatures*, 28(4), 369–376. doi:10.3184/096034011X13198126967382
- Tallman, D. J., Anasori, B., & Barsoum, M. W. (2013). A Critical Review of the Oxidation of Ti_2AlC , Ti_3AlC_2 and Cr_2AlC in Air. *Materials Research Letters*, 1(3), 115–125. doi:10.1080/21663831.2013.806364
- Tian, W., Wang, P., Kan, Y., & Zhang, G. (2008). Oxidation behavior of Cr_2AlC ceramics at 1,100 and 1,250 °C. *Journal of Materials Science*, 43(8), 2785–2791. doi:10.1007/s10853-008-2516-2
- Tian, W., Wang, P., Zhang, G., Kan, Y., & Li, Y. (2007). Mechanical Properties of Cr_2AlC Ceramics. *Journal of the American Ceramic Society*, 90(5), 1663–1666. doi:10.1111/j.1551-2916.2007.01634.x
- Tolpygo, V. K., Dryden, J. R., & Clarke, D. R. (1998). Determination of the growth stress and strain in $\alpha\text{-Al}_2\text{O}_3$ scales during the oxidation of Fe–22Cr–4.8Al–0.3Y alloy. *Acta Materialia*, 46, 927–937. doi:10.1016/S1359-6454(97)00306-6
- Walter, C., Sigumonrong, D. P., El-Raghy, T., & Schneider, J. M. (2006). Towards large area deposition of Cr_2AlC on steel. *Thin Solid Films*, 515(2), 389–393. doi:10.1016/j.tsf.2005.12.219
- Wang, Q. M., Flores Renteria, a., Schroeter, O., Mykhaylonka, R., Leyens, C., Garkas, W., & to Baben, M. (2010). Fabrication and oxidation behavior of Cr_2AlC coating on Ti6242 alloy. *Surface and Coatings Technology*, 204(15), 2343–2352. doi:10.1016/j.surfcoat.2010.01.002
- Wang, Q. M., Mykhaylonka, R., Flores Renteria, a., Zhang, J. L., Leyens, C., & Kim, K. H. (2010). Improving the high-temperature oxidation resistance of a $\beta\text{-}\gamma$ TiAl alloy by a Cr_2AlC coating. *Corrosion Science*, 52(11), 3793–3802. doi:10.1016/j.corsci.2010.07.031
- Woodford, D. A. (2006). Gas phase embrittlement and time dependent cracking of nickel based superalloys. *Energy Materials: Materials Science and Engineering for Energy Systems*, 1, 59–79. doi:10.1179/174892306X99679
- Zhu, D., & Miller, R. A. (1996). Evaluation of Oxidation Damage in Thermal Barrier Systems. NASA TM-107360, ARL-TR-125, 1–20.

